The simulation of a landslide-induced surge wave and its overtopping of a dam using a coupled ISPH model

Pengzhi Lin, Xin Liu & Jianmin Zhang

Taylor & Francis
Taylor & Francis Group

The simulation of a landslide-induced surge wave and its overtopping of a dam using a coupled ISPH model

Pengzhi Lin[a]*, Xin Liu[b] and Jianmin Zhang[a]

[a]State Key Laboratory of Hydraulics and Mountain River Engineering, Sichuan University, Chengdu, China; [b]College of Harbour Coastal and Offshore Engineering, Hohai University, Nanjing, China

In this paper, a landslide-induced surge wave and its overtopping of a dam is simulated using a coupled ISPH model. In the model, the mirror particle treatment was employed to simulate the moving structures and a particle symmetry criterion was enforced for free surface judgment. A telescopic boundary is presented for the landslide body motion treatment. The model is first used to simulate the two types of surge wave induced by submarine and aerial landslides and the simulation results are compared to the previously published experimental data. Then, in order to study landslide-induced wave propagation and especially the overtopping of a dam, laboratory experiments were conducted in which the landslide motion, the wave gauge results and the total overtopping volume were presented and compared to the numerical results. It was found that the present numerical model can accurately simulate the entire process of surge wave generation, propagation and overtopping of a dam.

Keywords: ISPH; landslide-induced waves; wave overtopping a dam; coupled body motion

1. Introduction

Landslide-induced tsunami have caused extensive loss of human life and devastating damage around the world. Besides the direct destruction to nearby towns, landslide masses collapse into reservoirs, costal areas, river channels or other shallow-water regions, which usually results in a huge surge wave – a landslide-induced surge wave. On 9 October 1963, a 300 million m³ landslide body slipped into the Vaiont reservoir in Italy, with an entry velocity of about 30 m/s. The maximum surge wave was about 260 m high from the reservoir water level, and 100 m high from the dam crest. The surge wave propagated 1.4 km within 7 minutes, killing 3000 people in five towns. Comparatively speaking, the landslide-induced surge wave has been more frequently observed in coastal area than on those in proximity to reservoirs. On 17 July 1998, a large tsunami was generated in Papua New Guinea after a M7.0 earthquake, destroying seven villages and taking 2200 lives. After the disaster, researchers found that both the arrival time and the large wave height could not be directly generated by an earthquake, and that underwater landslide might have been the main cause (Tappin, Watts, McMurtry, Lafoyd, & Matsumoto, 2001). This conclusion was supported by other studies (Okal, 2003). The largest tsunami recorded in history was the Lituya tsunami, which occurred on 9 July 1953 in Alaska, with a maximum run-up height

of 524 m. The main cause was also considered to be an earthquake-induced landslide (Fritz, 2001).

Since the complex generation process and propagation properties of the surge wave, many experimental studies had been conducted on the landslide-induced wave. Wiegel (1955) presented the results of his experiment in a 2D flume, in which he showed that the landslide surge wave might be more serious than that directly caused by the earthquake, and he suggest that people to pay more attention to this issue. Heinrich (1992) conducted a 2D experiment on the landslide surge wave, and a video camera was used to record the surge wave surface. In the experiment, two types of landslide body were studied, which resulted in two different surge wave profiles. In another 2D experiment presented by Walder, Watts, Sorensen, and Janssen (2003), the landslide body consisted of a triangular front and a rectangular tail, which made the body volume adjustable. 3D experiments have also been carried out (Grilli & Watts, 2005; Panizzo, De-Girolamo, & Petaccia, 2005), and researchers have found that the resistance from the liquid to landslide body is of paramount importance to surge wave generation (Grilli & Watts, 2005). Alongside experimental studies, numerical investigation has become increasingly popular and various numerical models have been presented. Lynett and Liu (2002) developed a Boussinesq model for this problem, in which they

used a predetermined bed deformation equation to represent the landslide motion. Watts, Grilli, Kirby, Fryer, and Tappin (2003) employed a hyperbolic cosine function to simulate the landslide motion, and their wave model was also based on the Boussinesq equation. Heinrich (1992) conducted a numerical study using his NASA-VOF2D model based on the Navier-Stokes (NS) equations. In this model, the motion of the landslide was set to be that recorded in the experiment, and a comparison between numerical and experimental results was presented. The numerical model for the landslide-induced wave requires skillful simulation of dynamic fluid-structure coupling and water wave propagation. In the above mesh-based models, the Lagrangian landslide body motion must be described in a Euler grid, and the movement of the body-fitted grid near the structure and the communication between the moving body and the Eulerian meshes obviously increase the algorithm complexity; as a result, a full Lagrangian model is necessary. Because of its Lagrangian and mesh-less features, smoothed particle hydrodynamics (SPH) is inherently well suited to the analysis of problems with a moving boundary and large free surface deformation (Monaghan, 1994). This method has been widely used in many hydrodynamics problems (Shao, 2009; Shao & Gotoh, 2004), but so far there has been little application of SPH to landslide surge wave simulation. Ataie-Ashtiani and Shobeyri (2008) developed an Incompressible SPH (ISPH) model for the simulation of a landslide-induced surge wave. In their simulation, they presented free surface deformation near landslide, wave run along a side wall, and the pressure field. Pastor, Haddad, Sorbino, Cuomo, and Drempetic (2009) used a depth-integrated SPH model for the 3D and large-scale problems.

The omissions in the previous studies lie in the following two aspects. Firstly, almost all of the SPH results in the literature are not focused on surge wave propagation (De-Girolamo et al., 2006; Panizzo, Cuomo, & Dalrymple, 2006; Panizzo & Dalrymple, 2004), which is the direct threat to hydraulic structures. The prediction of wave propagation and its *destructive power* are the primary goal of the numerical investigation, which relies on the accurate simulation of the fluid-landslide interaction. The second omission is that in almost all of the numerical studies, the landslide motion is treated as a known value or function. In these studies, the landslide motion is set as a measuring result (Sue, Nokes, & Davidson, 2011), a constant value or function (Enet, Grilli, & Watts, 2003), or calculated by a predesigned force-velocity relation (Guo & Wu, 2000). These treatments may obviously improve the results for the comparison between a simulation and its corresponding experiment. However, in real life, landslide motion is usually not known in advance. X. Liu, Xu, Shao, and Lin (2013) presented an ISPH model for the simulation of the motion of coupled structures in fluid; however, in their model, body contact between floating structure and fixed boundary was not allowed. Obviously, a landslide

simulation will inevitably involve body contact between the landslide and the side slope. In addition, although there have been many numerical models for the simulation of wave overtopping using both the grid-based method (P. Liu, Lin, Chang, & Sakakiyama, 1999; Reeve, Soliman, & Lin, 2008) and the particle-based method (Shao et al., 2006), the overtopping of a landslide surge wave is still rarely studied.

In this paper, a coupled ISPH model will be developed for the simulation of a landslide-induced surge wave. In our study, the ISPH method following X. Liu, Lin, and Shao (2014) was employed for treating the large free surface deformation and the complex fluid-solid coupling. The model was applied to a landslide entry case with a coupled landslide motion in order to verify the model performance on surge wave propagation and landslide motion. Finally, an experiment was conducted together with the numerical simulation, which focused on the surge wave generation, propagation and overtopping of a dam. A comparison is then made of the body motion, free surface deformation, wave gauge results and the total overtopping volume.

2. The ISPH model

2.1. *Governing equations*

NS equations are solved in this model for the free surface flow in fluid-solid coupling problems. In the ISPH method, NS equations are written in Lagrangian form and the advection term is automatically calculated through the tracking of particle motion, hence, the numerical diffusion arising from the successive interpolation of the advection function in Eulerian grid-based methods is controlled without the need for a sophisticated scheme. The mass and momentum conservation equations are written as

$$\nabla \cdot \vec{u} = 0, \tag{1}$$

$$\frac{d\vec{u}}{dt} = -\frac{1}{\rho}\nabla p + \vec{g} + \upsilon_0 \nabla^2 \vec{u} + \frac{1}{\rho}\nabla \cdot \vec{\tau}, \tag{2}$$

where $\vec{u}$ is the particle velocity vector, t is the time, ρ is the fluid density, p is the particle pressure, $\vec{g}$ is the gravitational acceleration vector, υ_0 is the laminar kinematic viscosity and $\vec{\tau}$ is the sub-particle scale (SPS) turbulence stress (Lo & Shao, 2002).

The eddy viscosity assumption is often used to model the SPS turbulence stress $\vec{\tau}$ as

$$\tau_{ij} = \rho \left(2\upsilon_t S_{ij} - \frac{2}{3}k\delta_{ij} \right), \tag{3}$$

where υ_t is the turbulence eddy viscosity, $S_{ij} = (\partial u_i/\partial x_j + \partial u_j/\partial x_i)/2$, k is the turbulence kinetic energy and δ_{ij} is the Kronecker delta function. Here the turbulence eddy viscosity υ_t is calculated using a modified Smagorinsky model

(Li, Troch, & Rouck, 2004),

$$v_t = (C_S d_0)^2 |S|, \tag{4}$$

where C_S is the Smagorinsky constant ($= 0.1$), d_0 is the particle spacing representing the characteristic length scale of the small eddies and $|S| = \sqrt{|2S_{ij} S_{ij}|}$, which is the local strain rate.

The two-step projection method is employed here to solve Equations (1) and (2) (Chorin, 1968). The computation is composed of two steps. The first step is an explicit integration of velocity in time without considering the pressure and gravity terms,

$$\vec{u}_* = \vec{u}_t + \left(v_0 \nabla^2 \vec{u} + \frac{1}{\rho} \nabla \cdot \vec{\tau} \right) \Delta t, \tag{5}$$

$$\vec{r}_* = \vec{r}_t + \vec{u}_* \Delta t, \tag{6}$$

where $\vec{u}_t$ and $\vec{r}_t$ are the particle velocity and position at time t, $\vec{u}_*$ and $\vec{r}_*$ are the intermediate particle velocity and position and Δt is the time increment.

Assuming that $\Delta \vec{u}_{**}$ is the changed particle velocity contributed by the remaining pressure and gravity terms,

$$\vec{u}_{t+1} = \vec{u}_* + \Delta \vec{u}_{**} = \vec{u}_* + \left(\vec{g} - \frac{1}{\rho} \nabla p_{t+1} \right) \Delta t. \tag{7}$$

Through combination with the mass conservation Equation (1), the Pressure Poisson Equation (PPE) is obtained as follows (X. Liu et al., 2013):

$$\nabla \cdot \left(\vec{g} - \frac{1}{\rho} \nabla p_{t+1} \right) = -\frac{\nabla \cdot \vec{u}_*}{\Delta t}. \tag{8}$$

After obtaining the pressure field, the particle velocity is updated by Equation (7) and the positions of the particles are centered in time as

$$\vec{r}_{t+1} = \vec{r}_t + \left(\frac{\vec{u}_t + \vec{u}_{t+1}}{2} \right) \Delta t. \tag{9}$$

2.2. ISPH formula

The viscous and turbulent stress terms in Equation (2) (Lo & Shao, 2002) are given as follows:

$$(v_0 \nabla^2 \vec{u})_i = \sum_j \left(\frac{4 m_j (\mu_i + \mu_j) \vec{r}_{ij} \cdot \nabla_i W_{ij}}{(\rho_i + \rho_j)^2 (|\vec{r}_{ij}|^2 + \eta^2)} \right) \vec{u}_{ij}, \tag{10}$$

$$\left(\frac{1}{\rho} \nabla \cdot \vec{\tau} \right)_i = \sum_j m_j \left(\frac{\vec{\tau}_i}{\rho_i^2} + \frac{\vec{\tau}_j}{\rho_j^2} \right) \cdot \nabla_i W_{ij}, \tag{11}$$

where i and j are a reference particle and its neighbor, m is the particle mass, W is the kernel function, μ is the dynamic viscosity and equal to ρv_0. $\vec{r}_{ij} = \vec{r}_i - \vec{r}_j$, $\vec{u}_{ij} = \vec{u}_i - \vec{u}_j$,

η is $0.1h$ to keep the denominator nonzero with h as the smoothing length, and $\nabla_i W_{ij}$ is the kernel gradient.

The pressure term (Khayyer & Gotoh, 2008, 2009) is expressed as

$$\left(\frac{1}{\rho} \nabla p \right)_i = \sum_j m_j \left(\frac{p_i}{\rho_i^2} + \frac{p_j}{\rho_j^2} \right) \nabla_i W_{ij}. \tag{12}$$

The velocity divergence in the right-hand side of Equation (8) (Khayyer, Gotoh, & Shao, 2009) is discretized as

$$-(\nabla \cdot \vec{u}_*)_i = \sum_j \frac{m_j}{\rho_j} (\vec{u}_{*i} - \vec{u}_{*j}) \cdot \nabla_i W_{ij}, \tag{13}$$

and the left-hand side of Equation (8) is expressed as

$$\nabla \cdot \left(\frac{1}{\rho} \nabla p \right)_i = \sum_j \frac{8 m_j}{(\rho_i + \rho_j)^2} \frac{p_{ij} \vec{r}_{ij}}{(|\vec{r}_{ij}|^2 + \eta^2)} \cdot \nabla_i W_{ij}, \tag{14}$$

where $p_{ij} = p_i - p_j$.

The choice of different kernel functions can greatly affect SPH performance, just like the different finite difference schemes in an Finite Different Method. In this proposed 2D ISPH model, the B-spline kernel function was employed (Monaghan & Pongracic, 1985):

$$W(q, h) = \begin{cases} \dfrac{15}{7\pi h^2} \left(\dfrac{2}{3} - q^2 + \dfrac{1}{3} q^3 \right) & 0 < q < 1.0 \\ \dfrac{15}{7\pi h^2} \left(\dfrac{1}{6} (2-q^3)^3 \right) & 1.0 < q < 2.0, \\ 0 & q \geq 2.0 \end{cases} \tag{15}$$

where $q = \left| \vec{r}_i - \vec{r}_j \right| / h$.

2.3. Boundary treatments

2.3.1. The mirror particle method

Since its first presentation in Cummins and Rudman (1999) for solid boundary simulation, the mirror particle treatment has been employed by many SPH researchers (X. Liu et al., 2013; Lo & Shao, 2002). X. Liu et al. (2014) developed this method for coupling structure motion simulation. In their treatment, boundary particles (mirror particles) are automatically generated according to the fluid particle parameters, even when the solid boundary changes its position. Compared to the other solid boundary particle treatment (Vandamme, Zou, & Reeve, 2011), this method does not require adjusting the position of boundary particles and the boundary motion parameters are adaptively included in the mirroring rules, which makes the numerical algorithm more straightforward. In this study, the treatment in X. Liu et al. (2014) is employed for the moving boundary treatment.

2.3.2. The modified landslide motion model

In general, there are three forces acting on the landslide body and determining its motion: the fluid force F_f, the supported force F_s and the gravity G, as shown in Figure 1(a). The landslide will slide down the inclination under external forces. In this study, the incline surface friction is ignored for simplicity. Following the treatment in X. Liu et al. (2014), the fluid pressure around the moving body will be integrated using the pressure integration procedure to get the fluid force F_f on the rigid body. In this problem, the body sliding direction of the landslide is perpendicular to the F_s direction, which means that supported force makes no contribution to the sliding velocity calculation. Therefore, only the resultant force on the direction of movement (the sliding direction) is needed for the calculation of the sliding acceleration

$$F_{\text{res}} = G^{\text{incline}} - F_f^{\text{incline}}, \qquad (16)$$

where G^{incline} and F_f^{incline} are the G and F_f components, respectively. F_{res} is the resultant force on the direction of movement.

In most studies on fluid-solid coupling using the SPH method, the moving boundary is not allowed to contact the fixed boundary (Oger, Doring, Alessandrini, & Ferrant, 2006). For landslide problems, the moving body slides along the inclination, which makes the moving boundary truncate the fixed boundary, as shown in Figure 1(b). In this situation, the fixed boundaries (L_1 and L_2) need to be stretched or compressed during the coupling. In Figure 1(b), from time t to time t', the end point L_{1e} of the upper fixed boundary will move to L_{1e}' (this boundary is stretched), while the start point L_{2s} of the lower fixed boundary will move to L_{2s}' (this boundary is compressed). Due to self-adaption, the mirror particles will adapt the

boundary deformation and generate or disappear in the deformed region. As shown in Figure 1(b), when the solid boundaries move from their old position (dashed) at time t to the new position (solid) at time t', the mirror particles (green hollow circles) near old boundaries disappear and new particles (green solid circles) generate near new boundaries to adapt fluid particles at time t'. With these procedures, the coupled motion of the landslide body can be well described.

2.3.3. The free surface treatment

On the free surface, the Dirichlet boundary condition '$p = \text{constant}$' should be added, where the constant is usually the atmospheric pressure (zero in this paper). Following X. Liu et al. (2014), the following judgments are used for the free surface treatment:

$$(\rho_{\text{number}})_i = \sum_j W(|\vec{r}_i - \vec{r}_j|, h)\mathrm{d}V, \qquad (17)$$

$$(\rho_{\text{sym}})_i = \sum_j \frac{m_j}{\rho_j} \frac{x_{ij} + z_{ij}}{\mathrm{d}_0} W(|\vec{r}_i - \vec{r}_j|, h), \qquad (18)$$

where ρ_{number} is the particle number density that is close to 1.0 in the inner fluid region, $\mathrm{d}V$ is the volume of the particle and $\mathrm{d}V = m_j/\rho_j$. When $\rho_{\text{number}} < 0.9$, the particle is classified as a surface particle. $x_{ij} = x_i - x_j$, $z_{ij} = z_i - z_j$. ρ_{sym} denotes the quantification of the particle distribution asymmetry, and the critical value is chosen as 0.1 for the inner fluid particle in the present model.

3. Model application

In this section, the present model will be applied to landslide-induced surge wave simulation. First, a similar
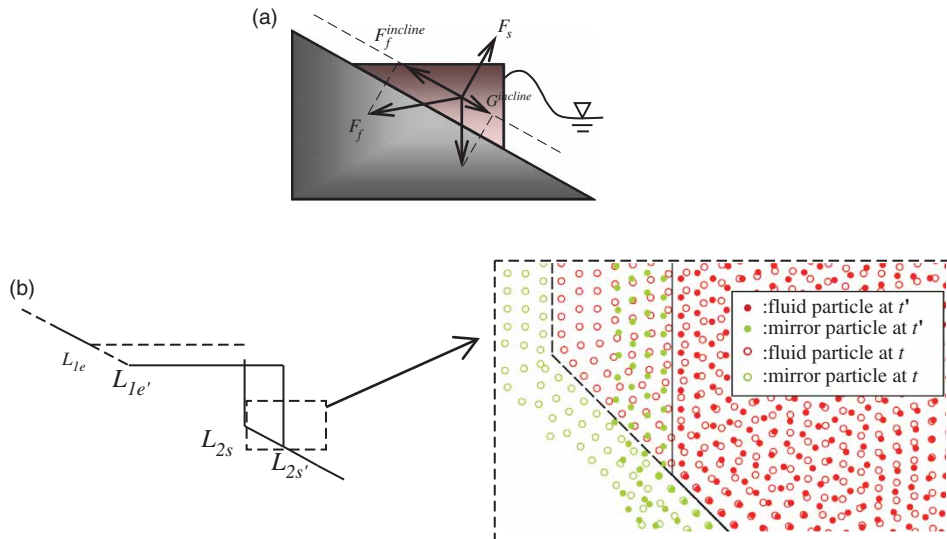

Figure 1. Landslide motion treatment: (a) fluid force calculation; (b) telescopic boundary and update of the mirror particles.
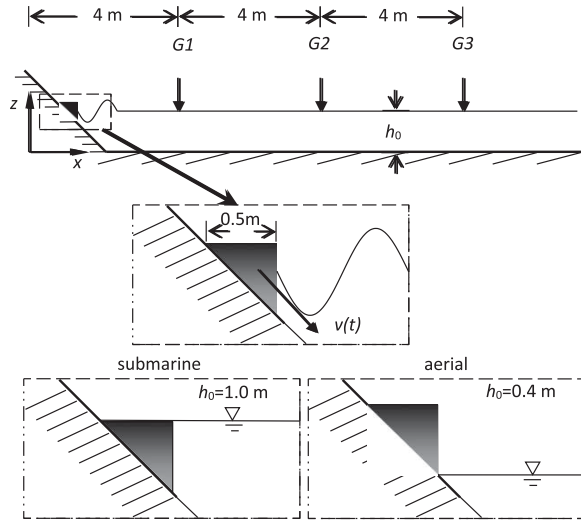
Figure 2.   Set-up of landslide simulation in Heinrich (1992).

3.1.   *The simulation of surge wave propagation*

In this section, the water entry of a landslide and its induced waves are simulated by the present ISPH coupling model for verification. This problem was studied experimentally and numerically by Heinrich (1992) and also by Ataie-Ashtiani and Shobeyri (2008) using a standard ISPH model. The box that modeled the landslide was triangular in cross section (0.5 m × 0.5 m) and has the same width as the flume. The physical experiment generated the water waves by allowing a rigid box to slide down an inclined plane with a 45° slope. Here two different experimental situations are considered: submarine and aerial landslides. For the submarine landslide, the surge wave was generated with the submerged geometrical top of the box parallel to the still water surface, while for the aerial landslide, the bottom of the box was initially placed above the still free-surface, generating an aerial landslide-induced wave. The coordinate origin is located at the bottom of the flume and the left end of the horizontal section of the flume was at (2.0, 0.0). The box motion was calculated in couple instead of that given by a predefined velocity. Three wave gauges (G1, G2 and G3) were placed at 4 m, 8 m, and 12 m from the coordinate origin, as shown in Figure 2, where h_0 is the still water depth.

In the submarine landslide simulation, the water depth $h_0 = 1.0$ m and the top of the box was initially 0.01 m below the free surface. While in the aerial landslide simulation the still water depth is fixed at $h_0 = 0.4$ m and the

bottom of the box is initially placed above the still water surface. The initial particle distance of two cases are both $d_0 = 0.02$ m and a total of 45,900 and 18,190 particles are used in the submarine and aerial cases, respectively. A variable time step is employed to accelerate computation time. In Heinrich's (1992) study, landslide motion simulation was attempted using the coupled model, but it was found that the landslide velocity would become unstable after 0.4 s due to the fluid incompressibility. Accordingly, they used a prescribed landslide motion obtained from the experiment to model the coupled structure motion. In the present model, the landslide motion will be calculated using the truly coupled method in which the body motion is computed by the fluid dynamics.

The computed motion of the landslide body is shown in Figure 3 and compared with the experimental data in Heinrich (1992). In both sets of results the body movement by ISPH is slightly faster than that in the experiment, which may be due to neglecting the friction effect. In the aerial landslide result, the discrepancy is found to be larger, which may be due to the smaller water depth and the lower number of SPH particles. Therefore, a high resolution case with $d_0 = 0.005$ m is presented, in which a smaller discrepancy is observed. In the simulation, the effect on surge wave propagation is negligible. In general, the comparison between the numerical and experimental results is accepted.

The computational surge wave profiles of the present ISPH model are shown in Figure 4(a)–4(f) at three different time intervals and compared with the experimental data presented by Heinrich (1992). In the numerical simulations, the moving landslide suddenly stopped when the leading edge of the box arrives at the flume bottom, similar to the effect in the experiment. From the figure, it is shown that the computed profiles of the surge wave compare well with the experimental data, except that some tiny differences are found at the water interface on the left slope wall and the cavity region over the top of solid boundary. Figure 5(a)–5(c) shows the ISPH computed free surface variations on wave gauge G1, G2 and G3 (solid line) for both submarine and aerial cases, compared with the experimental data (circle) and numerical results of Heinrich's study (triangle) using the mesh-based method. In the figure, the agreements on all three wave gauges are shown to be quite good. Moreover, for the wave phase comparison at wave gauge G2, the ISPH simulation achieved a much better accuracy than Heinrich's mesh-based method. In the case of the submarine landslide, the maximum surge wave appeared in the second phase, which was caused by the wave reflection from the left side of the flume, while in the case of the aerial landslide, the entry of the moving body directly caused the maximum surge wave that appeared in the first phase. By use of the proposed fluid-structure coupling model, accurate agreement between the ISPH and experimental results on surge wave propagations were obtained.

simulation as that in Heinrich (1992) is presented as the verification of the model accuracy, except that the landslide motion will be simulated in couple. After this, the experimental and numerical study are presented and the comparisons focus on surge wave propagation and overtopping.
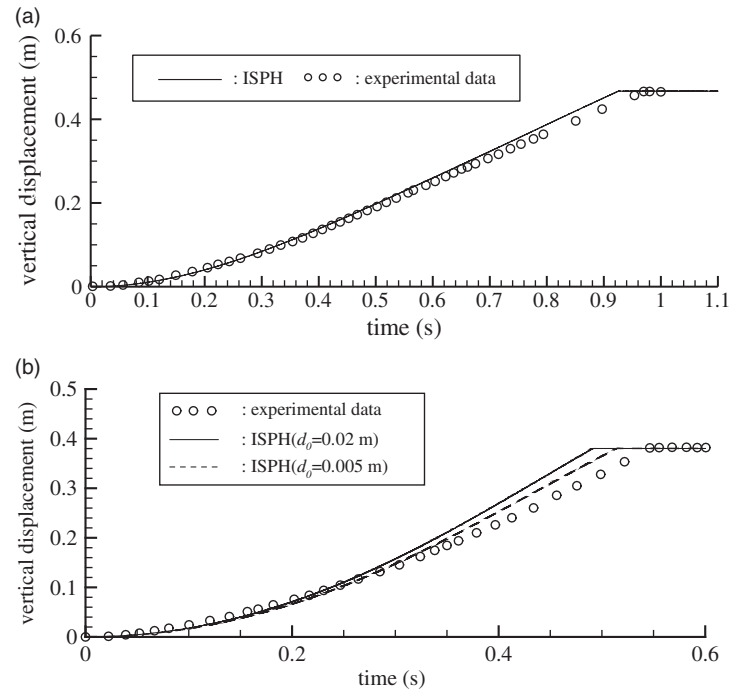
Figure 3.   Computed landslide motion of the ISPH model compared with the experimental data of Heinrich (1992) for (a) submarine landslide motion and (b) aerial landslide motion.
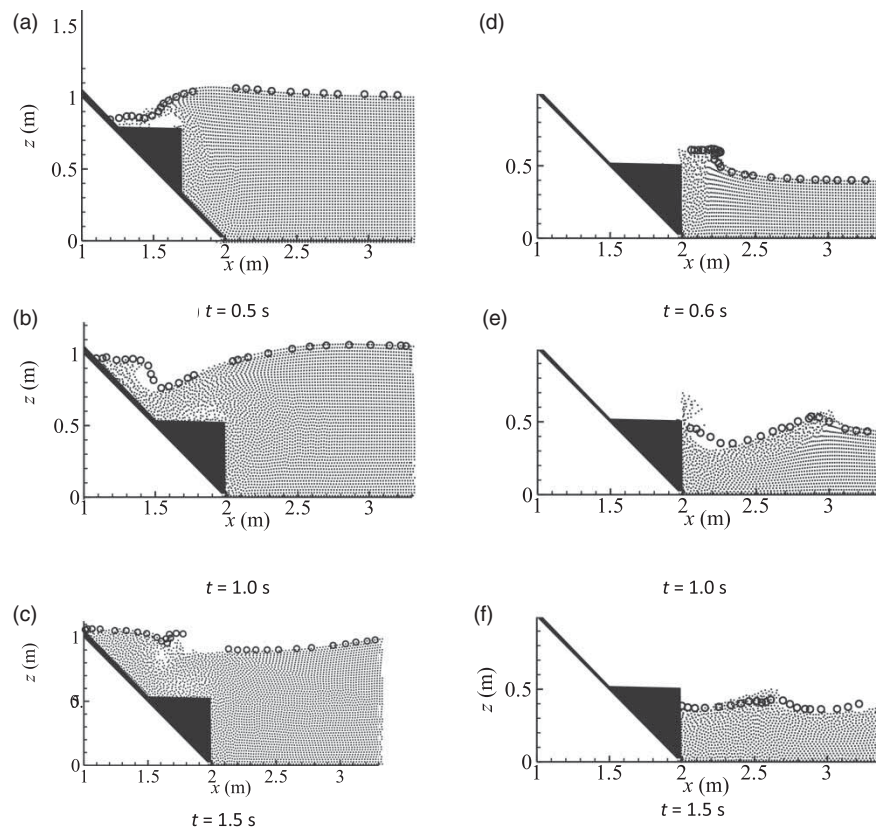

Figure 4.   ISPH computed surge wave profiles at 0.5 s (0.6 s), 1.0 s and 1.5 s, compared with the experimental data (circles) of Heinrich (1992) (a–c: submarine; d–f: aerial).
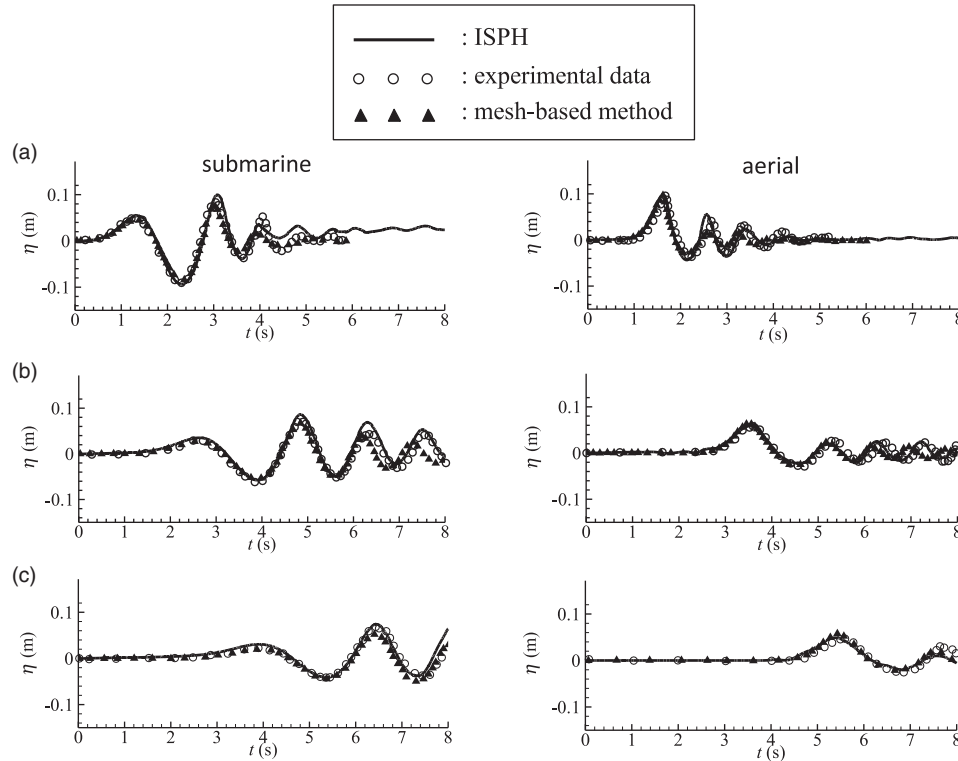
Figure 5. ISPH computed free surface elevations of submarine landslide at (a) $x = 4$ m, (b) $x = 8$ m and (c) $x = 12$ m, compared with the experimental data and mesh-based results (triangles) of Heinrich (1992).

3.2. Experimental and numerical study of coupling landslide-induced surge wave

In this section, the results of a laboratorial study on surge wave generation, propagation and its overtopping are presented for the verification of the present model. The coupling motion of the landslide body was simulated and compared with the experimental data, which is relatively rare in other similar studies, especially for the SPH method.

The experiment was conducted in the State Key Laboratory of Hydraulics and Mountain River Engineering, Sichuan University. Similar to Heinrich's (1992) set-up, the incline platform used to model the slope was fixed at the left side of the flume, as shown in Figure 6. The platform was made of board with an angle of 46° with respect to the horizon. The landslide body was made of PVC plat of a triangular geometric shape section. The horizontal and vertical edges were 251 mm and 260 mm, respectively. The two aluminum alloy guideways were embedded in the platform to connect the incline and the landslide body, which allowed the landslide to freely slide along the plat. The total mass of the sliding device was 55.9 kg. The area used for the experiment was 1.195 m wide, 8.0 m long and 1.0 m high (the total length of the flume was about 18.0 m). The still water depth $h_0 = 0.38$ m. The Plexiglas dam was fixed at the far end of the area and the detailed geometry is shown in Figure 6. A video camera was placed at the landslide section to record the body velocity, and three wave gauges were fixed at 1.6 m, 3.55 m and 6.55 m in the flume for the water surface elevation measurements. The bottom of the triangle section landslide was initially placed above the still water surface. At the beginning of the experiment, the landslide body slid down into the water, resulting in the large surface deformation. A buffer device was placed at the end of the guide 3 cm above the flume to prevent the landslide hitting the flume bottom. The surge wave propagated along the flume and finally impacted the dam, which led to the wave overtopping the dam. A water collecting device was placed behind the dam to measure the total volume of overtopped water.

In most studies on landslide-induced wave simulation (Ataie-Ashtiani & Shobeyri, 2008; Cremonesi, Frangi, & Perego, 2011), the landslide body motion was described by a prescribed time-velocity relation. In reality, however, the structure motion is usually unknown and is very hard to predict without the use of a dynamic-coupled model. In this section, the coupled motion of the landslide body will be modeled together with the surge wave propagation and overtopping. The calculation set-up is shown in Figure 6, as described in above paragraph. The initial particle distance was 0.005 m and a total of 106,680 water particles were employed. Two right-angled sides of the landslide body were designated as the moving boundary
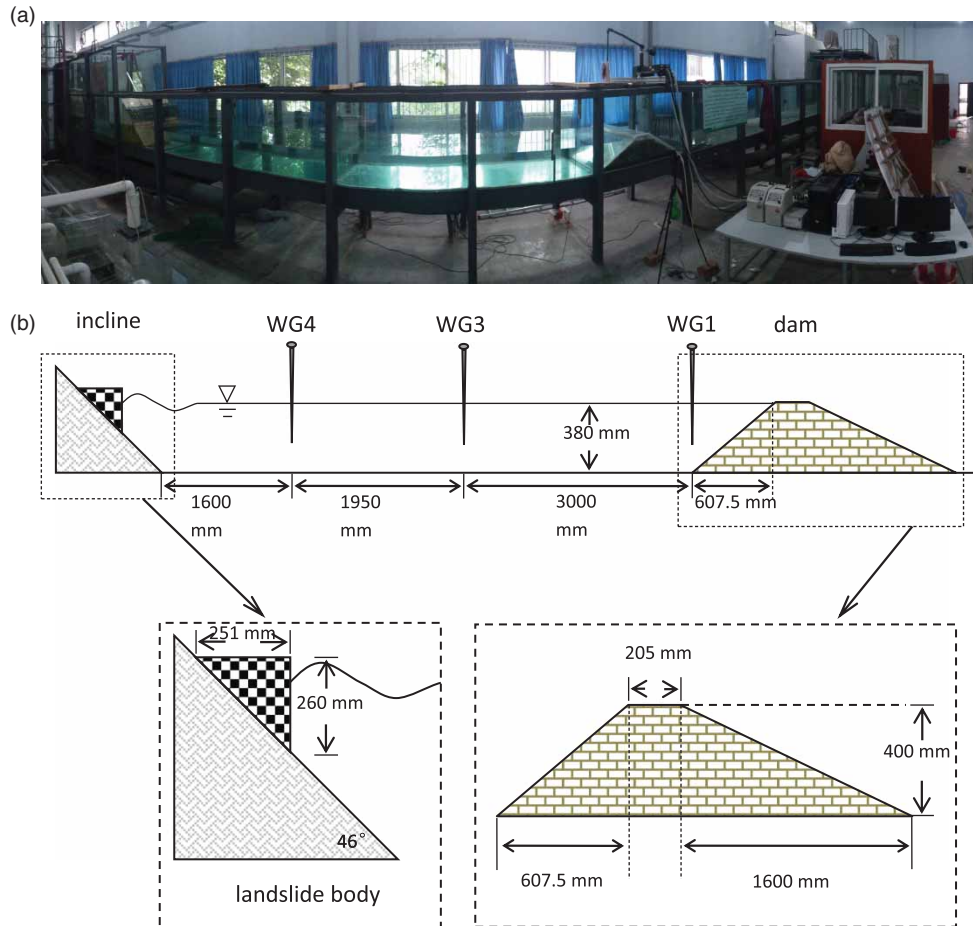
Figure 6.   Set-up of coupled landslide motion: (a) photograph of the experiment flume; (b) dimensions of the model.

and connected to the incline using the telescopic boundary mentioned in section 2.3.2.

The simulated surface profile and velocity field near the moving landslide are shown in Figure 7. At about $t = 0.5$ s, the landslide stopped due to hitting the buffer device on the flume bottom and a large surge wave was generated in front of the landslide. The water passed over the top side of the landslide and impacted the left incline, after which the surge wave reversed its direction with a wave breaking on the top, generating the second and third phases of the surge wave, etc. With the use of the surface symmetry criterion, Equation (18), a clear free surface profile will be observed and surface particle judgment will be improved. In the simulation, almost all of the surface particle errors near the solid boundary which may be mistakenly classified as surface particles by Equation (17) are corrected. The surface profile in the present model was clear and smooth. After the landslide entry into the water, the maximum fluid velocity occurred near to the solid body and free surface. The fluid velocity near the leading edge of the landslide caused the first surge wave propagated from the landslide to the dam, while the fluid velocity near the surface flowed over the landslide top and impacted the side slope. The reflection

wave broke on top of the landslide. It was observed that the maximum surge wave appeared in the first phase, which is the wave that will cause the largest damage.

In the simulation, the landslide motion was modeled interactively, in which the landslide velocity was updated by the fluid force dynamically. The time series of the landslide motion is shown in Figure 8 and compared with the experimental data recorded by video camera. It is seen from the figure that the difference between the numerical and experimental results is very slight. In terms of the accuracy prediction of the landslide motion, the landslide-induced surge wave was simulated well.

The free surface elevation at the three gauges is shown in Figure 9(a)–9(c) and compared with the experimental data. In the experiment, it was observed that only the first and second wave profiles were directly generated by the landslide body entry. Since the landslide motion was accurately simulated by the coupling model, the discrepancy between the numerical and experimental data for the first two waves is very small. A smaller amplitude was found for the third, fourth and fifth wave phases in the numerical results in comparison to the experimental data, while for the phase that occurred after 8 s the difference in wave
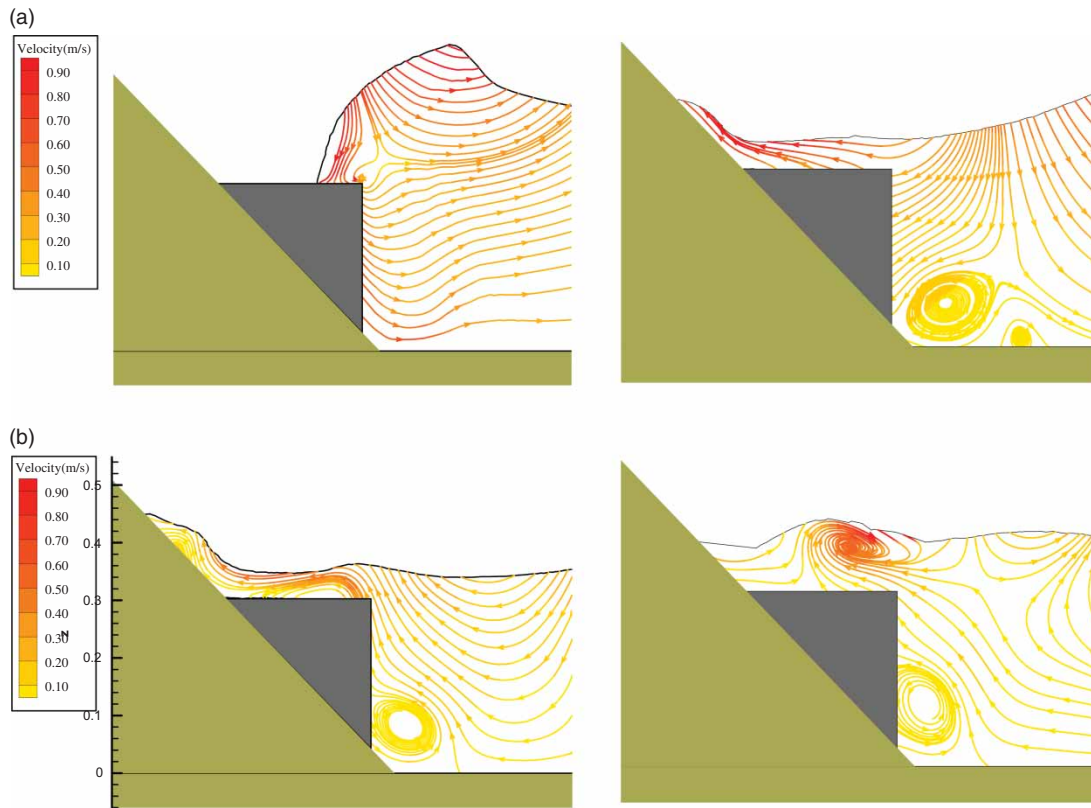
Figure 7. Surface profile and velocity field at time (a) 0.5 s, (b) 0.74 s, (c) 1.00 s and (d) 1.26 s.
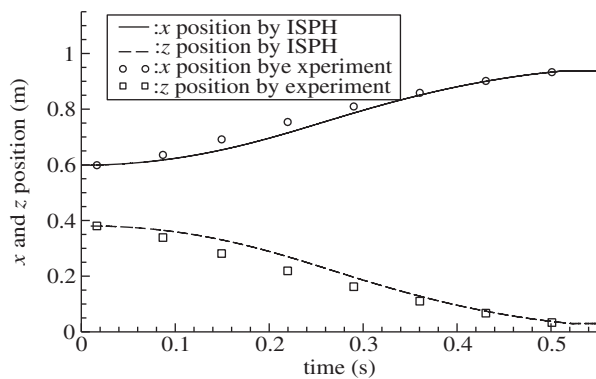

Figure 8. Landslide motion over time.

height is larger. This is probably due to the complex interactions between the incident wave, the reflected wave and the dam.

For the earth-rock dam, the overtopping volume of the surge wave is usually of paramount importance in dam risk assessment. The overtopping phenomena was simulated in the present model and is illustrated in Figure 10(a)–10(e). It was observed that the first surge wave approached the dam at about 3.0 s in Figure 10(b), together with a large overtopping volume. From 4.0 s to 4.6 s (Figure 10(c) and 10(d)), the wave crest passed over the dam and the water level in front of the dam reduced. It was found that the

largest overtopping velocity occurred at both sides of the dam surface, which may destroy the earth-rock dam. At about 6.1 s, the second surge wave approached the dam and similar overtopping was observed (Figure 10(e)). During the second surge wave overtopping, the wave run up and overtopping volume were significantly less than the first wave, but a large overtopping velocity was still observed. The results were similar for the rest of the waves and the dam surface was continually scoured.

Inthe experiment, the overtopping water was collected by a water-collecting device and the total volume was measured after the experiment. In the present simulation, the Lagrangian particles flowing over the left side of the dam crest were summed into the overtopping volume and this volume was recorded over time. Figure 11 shows the overtopping results in the simulation (the solid line C-1). From the figure, it is observed that the first surge wave approached the dam at about 3.0 s and flowed over, and this phenomenon can also be observed in Figure 10. The total overtopping volume was caused by about six waves, of which the first wave contributes the primary flow rate. As shown in the line C-1 in the figure, more than 80% of the overtopping volume was collected before 6.5 s, which shows that the largest damage is usually caused during the first and second wave phases. The wave overtopping finished after six or seven wave phases, and a total of 13.789 L water was recorded as having overtopped the dam. The
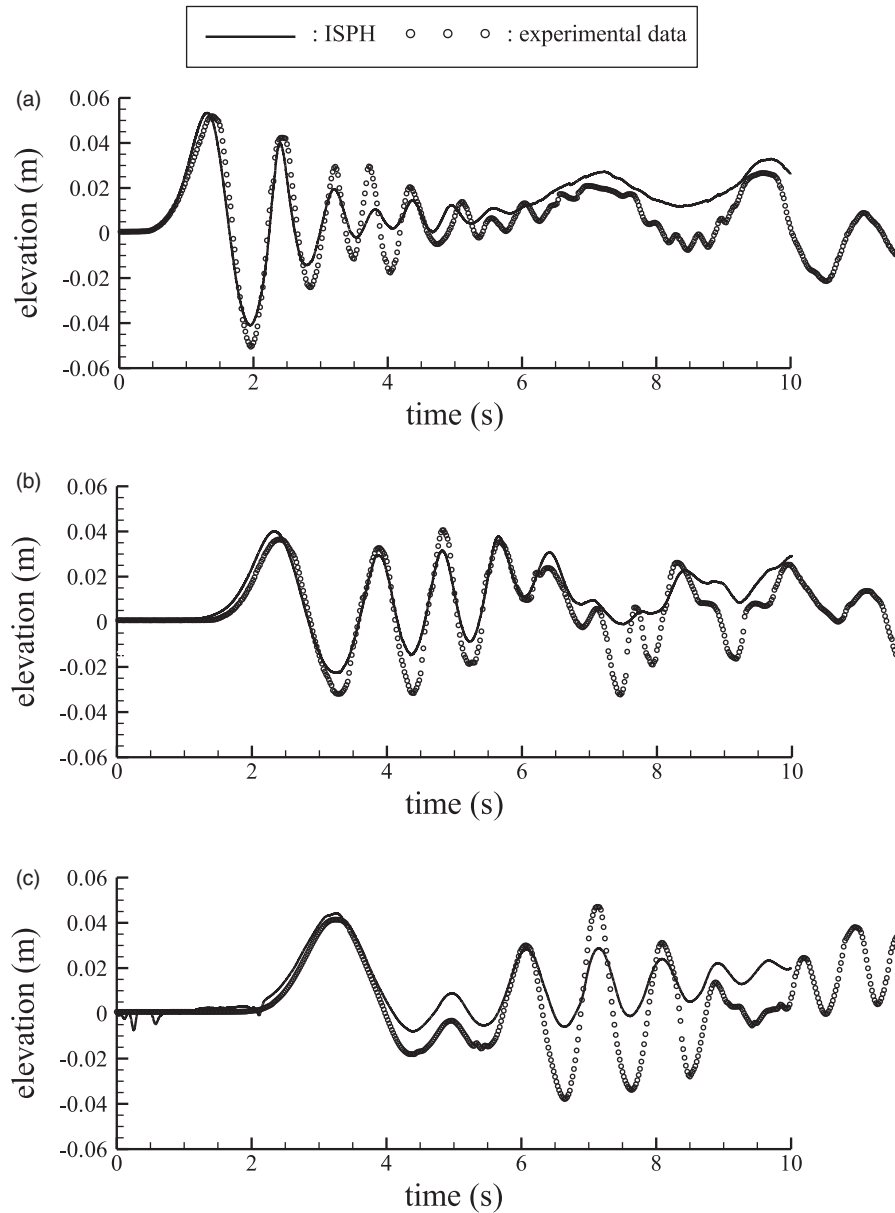
Figure 9.   Free surface elevation comparison between ISPH and the experimental data at (a) wave gauge 4, (b) wave gauge and (c) wave gauge 1.

difference between the numerical and experimental results is acceptable, although a lower total volume was obtained in the simulation. This discrepancy may due to calculating errors in the later stages of the surge wave. Fortunately, this effect is very small because that these late stage waves make a very small contribution to the overtopping volume.

After verifying the accuracy of the numerical model, additional cases were simulated with different landslide positions and still water depths in order to investigate their effect on overtopping volume. These parameters are presented in Table 1 in four additional cases (C-2 to C-5), while the overtopping volume results are illustrated in Figure 10. From the simulation results, it is found that for a higher position landslide (C-2 and C-3), the total overtopping volume increases, but the difference is relatively small. This is because more violent surge wave breaking happens for higher landslide impactions, which may dissipate more energy. However, for the deeper water depth (C-4 and C-5), the total volume obviously increases. Similar to the result in C-1, most of the overtopping volume is caused by the first two or three wave phases, especially for C-1 to C-3. From the above results, it is known that most of the surge wave damage is caused by the first few surge waves, and for the same landslide body, there is a greater risk with a deeper reservoir.
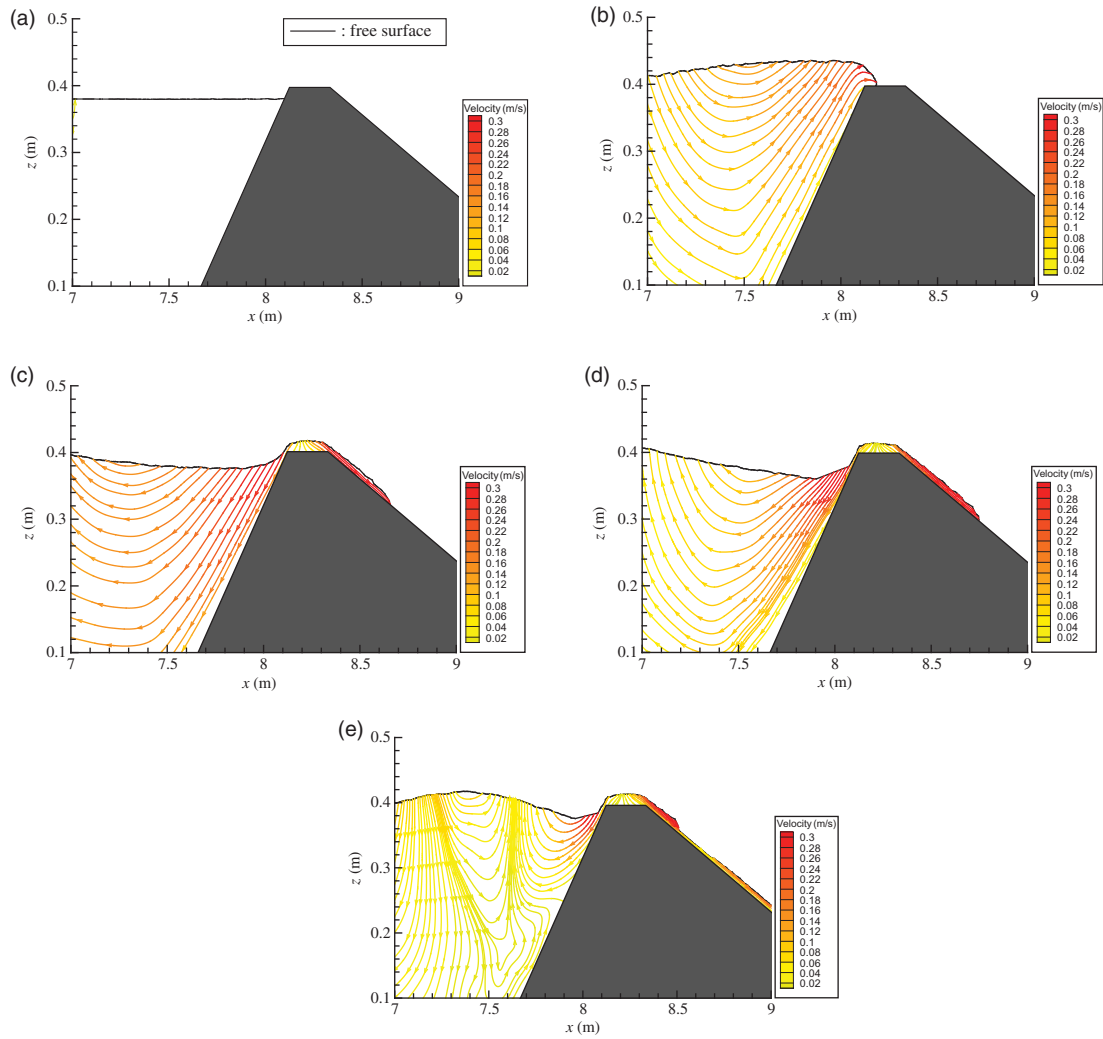
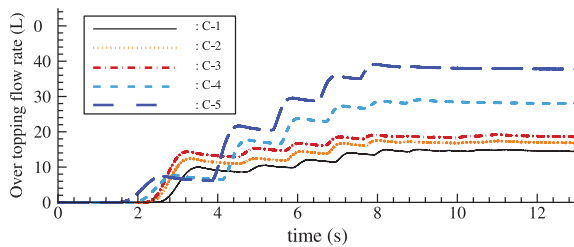Figure 10. Surge wave overtopping of the dam.

Figure 11. Overtopping flow rate by present ISPH model for five cases C-1 to C-5 (the total overtopping volume for C-1 recorded in the experiment is 13.789 L).

Table 1. Landslide position and still water depth in overtopping simulation cases.

Case	Landslide vertical offset from C-1 (m) h_l	Still water depth (m) h_0
C-1	0.000	0.38
C-2	0.095	0.38
C-3	0.190	0.38
C-4	0.000	0.57
C-5	0.000	0.76

4. Conclusions

In this paper, a landslide-induced surge wave and its overtopping of a dam were investigated using a coupled ISPH model in which all of the landslide body motions were simulated using the mirror particle treatment and a telescopic boundary was presented for the body sliding simulation.

In landslide-induced surge wave investigation, coupled motion was simulated using the present model to verify model accuracy, in which submarine and aerial landslide bodies ware modeled. Good results were obtained in the comparison with the experimental data on landslide body motion and wave propagation. Finally, both experimental and numerical investigations were carried out to investigate the surge wave generation, together with the wave overtopping of a dam. Good comparisons were achieved for the landslide body motion and acceptable results were obtained for the wave propagation and wave overtopping, which proves the present model's performance in the simulation of landslide-induced surge waves.

References

Ataie-Ashtiani, B., & Shobeyri, G. (2008). Numerical simulation of landslide impulsive waves by incompressible smoothed particle hydrodynamics. *International Journal of Numerical Methods in Fluids*, *56*, 209–232.

Chorin, A. J. (1968). Numerical solution of the Navier-Stokes equations. *Mathematics of Computation*, *22*, 745–762.

Cremonesi, M., Frangi, A., & Perego, U. (2011). A Lagrangian finite element approach for the simulation of water-waves induced by landslides. *Computers and Structures*, *89*, 1086–1093.

Cummins, S. J., & Rudman, M. (1999). An SPH projection method. *Journal of Computational Physics*, *152*, 584–607.

De-Girolamo, P., Wu, T. R., Liu, P. L. F., Panizzo, A., Bellotti, G., & Di-Risio, M. (2006). *Numerical simulation of three dimensional Tsunamis water waves generated by landslides: Comparison between physical model results, VOF, SPH and depth-integrated models*. ICCE Conference, San Diego.

Enet, F., Grilli, S. T., & Watts, P. (2003). *Laboratory experiments for tsunamis generated by underwater landslides: Comparison with numerical modeling*: Proceedings of the Thirteenth (2003) International Offshore and Polar Engineering Conference. Vol 3. Cupertino: International Society Offshore&Polar Engineerings, 372–379.

Fritz, H. M. (2001). Lituya bay case rockslide impact and wave run-up. *Science of Tsunami Hazards*, *19*(1), 3–22.

Grilli, S. T., & Watts, P. (2005). Tsunami generation by submarine mass failure. I: Modeling experimental validation, and sensitivity analyses. *Journal of Waterway, Port, Coastal and Ocean Engineering*, *131*(6), 283–297.

Guo, H. W., & Wu, C. C. (2000). Reservoir landslide generated wave model and its application. *Journal of North China Institute of Water Conservancy and Hydroelectric Power*, *21*(1), 24–27. (in chinese).

Heinrich, P. (1992). Nonlinear water waves generated by submarine and aerial landslides. *Journal of Waterway, Port, Coastal and Ocean Engineering*, *118*, 249–266.

Khayyer, A., & Gotoh, H. (2008). Development of CMPS method for accurate water-surface tracking in breaking waves. *Coastal Engineering Journal*, *50*(2), 179–207.

Khayyer, A., & Gotoh, H. (2009). Modified moving particle semi-implicit methods for the prediction of 2D wave impact pressure. *Coastal Engineering*, *56*(4), 419–440.

Khayyer, A., Gotoh, H., & Shao, S. D. (2009). Enhanced predictions of wave impact pressure by improved incompressible SPH methods. *Applied Ocean Research*, *31*, 111–131.

Li, T. Q., Troch, P., & Rouck, J. D. (2004). Wave overtopping over a sea dike. *Journal of Computational Physics*, *198*, 686–726.

Liu, P. L.-F., Lin, P., Chang, K.-A., & Sakakiyama, T. (1999). Numerical modeling of wave interaction with porous structures. *Journal of Waterway, Port, Coastal, and Ocean Engineering*, *125*(6), 322–330.

Liu, X., Lin, P. Z., & Shao, S. D. (2014). An ISPH simulation of coupled structure interaction with free surface flows. *Journal of Fluids and Structures*, *48*, 46–61.

Liu, X., Xu, H. H., Shao, S. D., & Lin, P. Z. (2013). An improved incompressible SPH model for simulation of wave-structure interaction. *Computers and Fluids*, *71*, 113–123.

Lo, E. Y. M., & Shao, S. D. (2002). Simulation of near-shore solitary wave mechanics by an incompressible SPH method. *Applied Ocean Research*, *24*, 275–286.

Lynett, P., & Liu, P. (2002). A numerical study of submarine-landslide-generated waves and run-up. *Proceedings of the Royal Society of London Series a-Mathematical Physical and Engineering Sciences*, *458*(2028), 2885–2910.

Monaghan, J. J. (1994). Simulating free surface flow with SPH. *Journal of Computational Physics*, *110*, 399–406.

Monaghan, J. J., & Pongracic, H. (1985). Artificial viscosity for particle methods. *Applied Numerical Mathematics*, *1*, 187–194.

Oger, G., Doring, M., Alessandrini, B., & Ferrant, P. (2006). Two-dimensional SPH simulations of wedge water entries. *Journal of Computational Physics*, *213*, 803–822.

Okal, E. A. (2003). T waves from the 1998 Papua New Guinea earthquake and its aftershocks: Timing the tsunamigenic slump. *Pure and Applied Geophysics*, *160*(10–11), 1843–1863.

Panizzo, A., Cuomo, G., & Dalrymple, R. A. (2006). *3D-SPH simulation of landslide generated waves*. ICCE 2006 Conference, San Diego.

Panizzo, A., & Dalrymple, R. A. (2004). *SPH modelling of underwater landslide generated waves*. ICCE 2004 Conference, Lisbon.

Panizzo, A., De-Girolamo, P., & Petaccia, A. (2005). Forecasting impulse waves generated by subaerial landslides. *Journal of Geophysical Research: Oceans*, *110*(C12).

Pastor, M., Haddad, B., Sorbino, G., Cuomo, S., & Drempetic, V. (2009). A depth-integrated, coupled SPH model for flow-like landslides and related phenomena. *International Journal for Numerical and Analytical methods in Geomechanics*, *33*, 143–172.

Reeve, D. E., Soliman, A., & Lin, P. (2008). Numerical study of combined overflow and wave overtopping over a smooth impermeable seawall. *Coastal Engineering*, *55*, 155–166.

Shao, S. D. (2009). Incompressible SPH simulation of water entry of a free-falling object. *International Journal of Numerical Methods in Fluids*, *59*, 91–115.

Shao, S. D., & Gotoh, H. (2004). Simulating coupled motion of progressive wave and floating curtain wall by SPH-LES model. *Coastal Engineering Journal*, *46*(2), 171–202.

Shao, S. D., Ji, C., Graham, D. I., Reeve, D. E., James, P. W., & Chadwick, A. J. (2006). Simulation of wave overtopping by an incompressible SPH model. *Coastal Engineering*, *53*(9), 723–735.

Sue, L. P., Nokes, R. I., & Davidson, M. J. (2011). Tsunami generation by submarine landslides: Comparison of physical and numerical models. *Environmental Fluid Mechanics*, *11*(2), 133–165.

Tappin, D. R., Watts, P., McMurtry, G. M., Lafoyd, Y., & Matsumoto, T. (2001). The Sissano, Papua New Guinea tsunami of July 1998 – offshore evidence on the source mechanism. *Marine Geology*, *175*(1), 1–23.

Vandamme, J., Zou, Q. P., & Reeve, D. E. (2011). Modeling floating object entry and exit using smoothed particle hydrodynamics. *Journal of Waterway, Port, Coastal and Ocean Engineering*, *137*(5), 213–224.

Walder, J. S., Watts, P., Sorensen, O. E., & Janssen, K. (2003). Tsunamis generated by subaerial mass flows. *Journal of Geophysical Research*, *108*(B5).

Watts, P., Grilli, S. T., Kirby, J. T., Fryer, G. J., & Tappin, D. R. (2003). Landslide tsunami case studies using a boussinesq model and a fully nonlinear tsunami generation model. *Natural Hazards and Earth System Science*, *3*, 391–402.

Wiegel, R. L. (1955). Laboratory studies of gravity waves generated by the movement of a submerged body. *American Geophysical Union-Transaction*, *36*(5), 759–774.